Formation of magnesium silicate hydrate cement in nature

Lisa de Ruiter* and Håkon Austrheim

Physics of Geological Processes (PGP), Department of Geosciences, University of Oslo, PO Box 1048, Blindern, 0136 Oslo, Norway

**Correspondence (l.d.ruiter@fys.uio.no)*

Abstract: Tillite lithified by magnesium silicate hydrate (M-S-H) cement has been formed at the surface of the Feragen Ultramafic Body in SE Norway. Serpentinization of olivine-rich rocks led to formation of brucite that dissolves during weathering to form a high pH (>9) Mg-rich fluid. This fluid dissolves quartz deposited by glaciers during the Weichselian glaciation. Subsequent evaporation leads to the precipitation of a nanocrystalline magnesium silicate hydrate phase with the approximate composition $Mg_8Si_8O_{20}(OH)_8 \cdot 6H_2O$. The resulting cemented rock is characterized by disintegrated and partly dissolved quartz grains that are surrounded by the M-S-H cement. This process occurs at surface conditions in a subarctic climate and is known to take place on the timescale of a few decades, as constrained by mining activities. Magnesium-based cement is currently of high interest as the search for environmentally friendly cement is a pressing task considering that the widely used Portland cement accounts for about 7% of the worldwide anthropogenic CO_2 emission. As this study provides new key insights into the formation process of natural CO_2-neutral magnesium-based cement on the field- and microscale, it could contribute in the development of a new sustainable construction material.

Introduction

Cementation is a prominent process in nature which leads to the lithification of sediments by chemical precipitation. The composition of the cement is highly dependent on the dissolution processes that take place in the system since this determines the chemistry of the fluid from which the cement will precipitate (Alonso-Zarza 2003; Elango & Kannan 2007; Sauer *et al.* 2015). Hence, weathering is essential in the cementation process. This is particularly evident at the Feragen Ultramafic Body (FUB), a serpentinized ultramafic complex in SE Norway close to Røros, where cementation takes place at the surface with a magnesium silicate hydrate phase. Since ultramafic material is far out of equilibrium at the surface it is prone to weathering when in contact with water and air. This is a well-studied process as it is of interest to

CO_2 sequestration (Cipolli *et al.* 2004; Hansen *et al.* 2005; Hänchen *et al.* 2008; Kelemen & Matter 2008; Wilson *et al*. 2009; Beinlich *et al.* 2010, 2012; Hövelmann *et al.* 2011; Oskierski *et al.* 2013), and also the reason for earlier research at the FUB (Beinlich & Austrheim 2012). This ultramafic complex is accordingly weathered and displays an extensive fracture network with reaction rims despite its location in a subarctic climate (Ulven *et al.* 2017). Furthermore, the FUB is partly covered with glacial till deposits that contain quartzofeldspatic material, emplaced during the Weichselian glaciation. The presence of felsic glacial deposits in the weathering zone of ultramafic material creates a unique geochemical system which allows mineral-fluid reactions involving minerals that are usually incompatible in nature. Therefore, the cement lithifying the tillite at Feragen is expected to have a unique composition and contain both ultramafic and felsic clasts.

Natural magnesium silicate hydrate cement has to our knowledge not been described before, but is well-known in the cement industry as M-S-H (magnesium silicate hydrate) cement. The production of Portland-based cement, the most common type of building cement which primarily hardens due to the precipitation of C-S-H (calcium silicate hydrate), accounts for 7% of the total anthropogenic CO_2 emission and is therefore the second largest source of anthropogenic CO_2 (IPCC 2005). The growing environmental concerns have made the search for an environmentally friendly alternative a state of the art research topic (Schneider *et al.* 2011; Imbabi *et al.* 2012). M-S-H cement has the potential to be a sustainable alternative for Portland cement and moreover to be suitable cement for the encapsulation of nuclear waste (Wei *et al.* 2011; Zhang *et al.* 2012, 2014; Jin & Al-Tabbaa 2014; Walling & Provis 2016). However, M-S-H is not commercially produced since an energy-efficient industrial manufacturing process has not been invented and fundamental information is lacking.

Here, we investigate the microstructures and petrology of the tillite and in particular the chemistry and formation history of the M-S-H cement that has been formed at the Feragen ultramafic complex. Note that we use the term cement in a geological way, thus meaning a hardened binder phase, and not in the industrial way, where it is defined as a dry unreacted powder. Since the formation of the M-S-H cement occurred at the Earth's surface without heating or the involvement of a carbon phase, analysing it in detail and unravelling the parameters controlling its formation history could give new insights that could contribute in the search for environmentally friendly cement. Moreover, this study describes a special geological system in which, up until now, an undiscovered chemical sediment forms.

Geological setting and climate

The Feragen Ultramafic Body crops out over an area of approximately 15 km^2, located 25 km east of Røros in SE Norway (Fig. 1). The FUB is identified as an alpine peridotite body and is one of multiple ultramafic complexes located on an approximately 200 km long transect (Moore & Hultin 1980). Hyperextension of the Baltic margin has been interpreted as the process responsible for the emplacement of some of these ultramafic bodies (Andersen *et al.* 2012). The FUB consists of alternating layers of dunite and peridotite, varying from lherzolite to harzburgite, which have a thickness ranging from a few cm to multiple m. Layers of chromitite are also present and are the reason for mining activities in the area which ceased around 1927. Varying degrees of serpentinization have altered the ultramafic body. Especially at the outer boundaries of the body, the rocks are highly serpentinized, while the inner parts are only partly serpentinized. Additionally, serpentine veins are abundant in the dunite layers, while andradite veins are present in the lherzolite layers (Plümper *et al.* 2014).

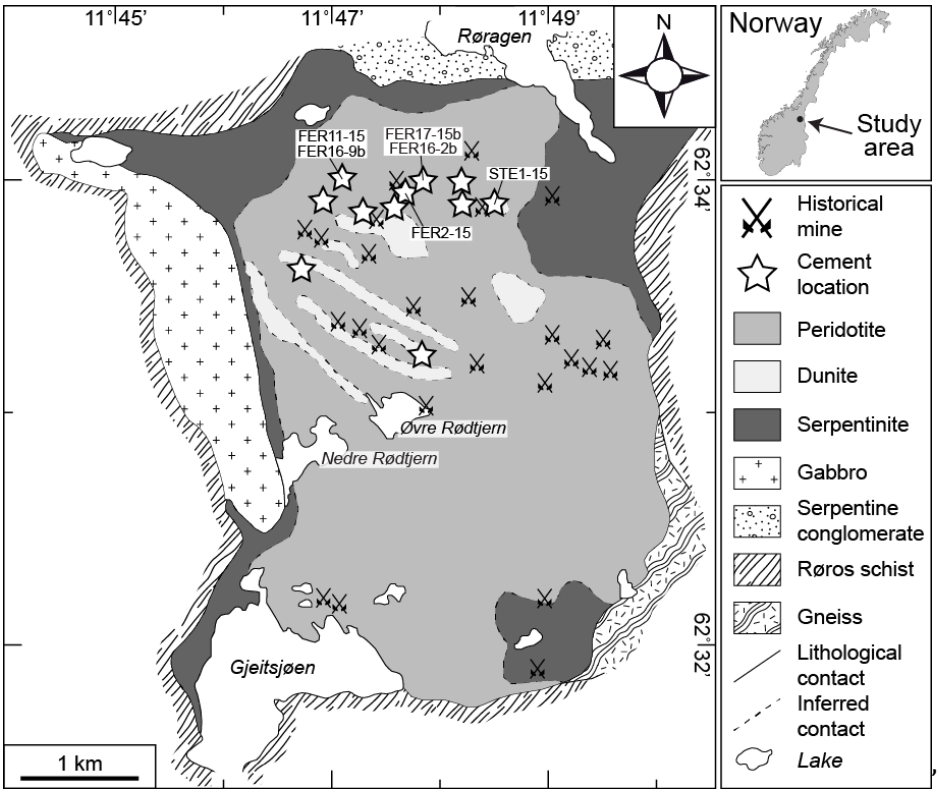

***Fig. 1**. Simplified geological map of the Feragen ultramafic complex showing the locations where the cemented rocks are found (after Moore & Hultin 1980; Beinlich & Austrheim 2012).*

The higher parts of FUB are almost completely exposed while the lower parts are partly covered by soil. The region has a subarctic climate, with temperatures below zero and snow covering the area during approximately half of the year. It is one of the coldest areas in Norway, with an average temperature of -6 °C in winter and 10 °C in summer. In autumn and spring, the temperature fluctuates around zero so that freeze-thaw cycles are common. The mean annual precipitation is 500 mm, which means it is one of the drier areas in Norway. However, during spring, water accumulates due to the melting of snow (climate data from the Norwegian Meteorological Institute). The subarctic climate results in soil processes such as frost heave which induces solifluction and mass movement. The topographical relief of the area enhances the fluid flow and mass movements, with the highest point on the FUB being 950 m above sea level, while the lakes Feragen and Røragen, which are located on the north and east side next to the FUB, are located approximately 300 m lower.

Field relationship

The FUB displays a cm-thick weathering rind and has extensive fractures where the weathering penetrates tens of cm into the rocks. Unsorted and unconsolidated felsic glacial sediment, known as till, is deposited on top of the ultramafic body and mixed with ultramafic rock fragments. These deposits vary from fine sand to boulders and are a remnant of the last glaciation; the Weichselian glaciation, which ended 11.7 ka. The exact source of the till is unknown as glaciers can transport rocks for many kilometres. The ultramafic fragments in the till constitute serpentinized peridotite and dunite like the FUB itself, while the felsic material mainly consists of quartz, feldspar and mica. The fine grained till locally forms polygonal patterns, which is a typical form of patterned ground in areas where frost heave occurs.

M-S-H cement lithified the till at multiple localities and turned it into a solid sedimentary rock with felsic and ultramafic clasts. The cementation is limited to the upper 10 to 30 cm of the surface and to several locations of a few m^2 each, which are indicated in Fig. 1. The cemented till occurs in three different settings: (1) at the trench walls of ancient mine entrances; (2) as boulders consisting entirely of cemented till; or (3) as thin layers on the surface. The mine shafts are cut into the ultramafic body and, therefore, the bottom of the trench wall in front of the shaft consists of fractured ultramafic rock, while the upper part is cemented till as shown in Fig. 2a. The cementation is limited to the outer 30 cm of the wall and thus the till is unconsolidated behind this. In the second setting, boulders of tillite up to 80 cm across occur partly buried in the soil at flat areas below slopes (Fig. 2b). Usually signs of soil movement like cracks and terraces occur around the boulders. In the third setting, the thin, crust-like, layers are 3 mm to 1 cm thick and form on top of the surface. This mainly occurs at flat areas that display the polygonal soil patterns (Fig. 2c), or on the

downhill side behind boulders on an inclined surface (Fig. 2d). Samples of the cemented tillite were collected for analysis from the different locations and settings. In addition, several samples of the peridotite with the weathering rind were studied.

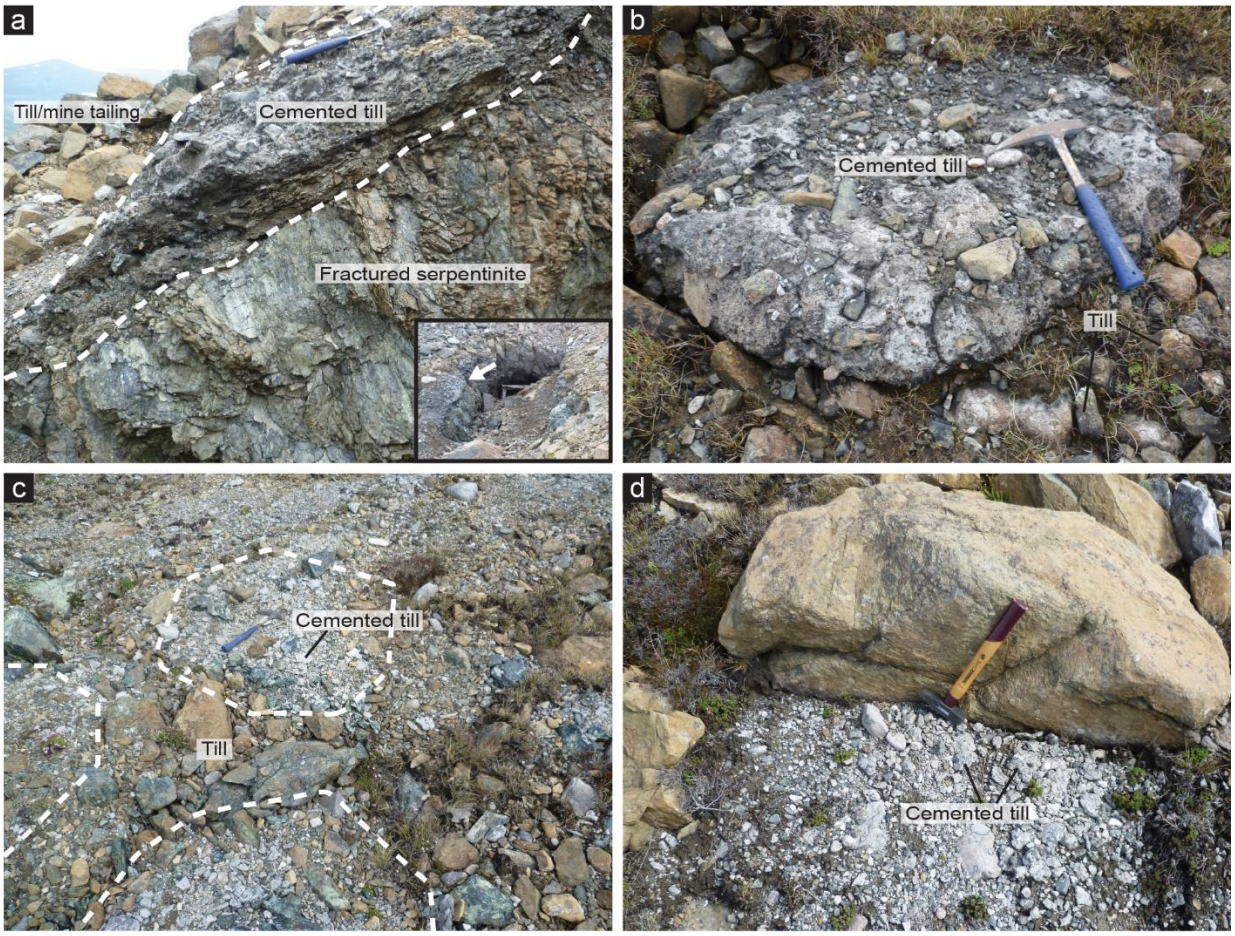

***Fig. 2**. Field pictures showing the occurrence of the M-S-H cemented rocks. (**a**) The trench wall of a mine which is cut into the ultramafic rock consists of cemented till at the upper part as outlined with the dashed lines. Behind the approximately 30 cm thick cemented layer, unconsolidated sediments are present. The small picture indicates the location of the cemented wall in relation to the mine. (**b**) A boulder of cemented till partly buried in the soil in an area where signs of soil movements like cracks and terraces are present. (**c**) Thin layers of 3 mm to 1 cm thick cemented fine grained till occur where soil patterns are present as indicated by the dashed lines, which are characterized by course till at the boundaries and fine till in the centres. (**d**) Thin layers of cemented till on the downhill side behind a boulder.*

Methods

The samples were investigated with multiple analytical techniques to observe their microstructures and obtain their chemical compositions. Polished thin sections were prepared to analyse the microstructures using optical microscopy with plane polarized light. Scanning electron microscopy (SEM) was used to obtain backscatter electron images (BSE), using the Hitachi SU5000 FE-SEM (Department of Geosciences, University of Oslo, Norway) operating with an acceleration voltage of 15 kV. Electron microprobe (EMP) analysis was performed with the Electron microprobe Cameca SX100 (Department of Geosciences, University of Oslo, Norway) to obtain the chemical composition of the material and to make chemical maps. To avoid evaporation of the hydrous content of the cement a spot size of 5 μm and a beam current of 5 nA were used to lower the beam damage. For the other phases, a beam current of 10 nA and a focussed beam were used. Powder X-ray diffraction (XRD) measurements of powdered ultramafic samples were conducted with the Bruker D8 Discover diffractometer at a wavelength of 1.5406 Å with Cu Kα1 radiation (Department of Chemistry, University of Oslo, Norway). High resolution synchrotron powder XRD measurements of powdered tillite samples were conducted at a dedicated beamline ID22 of the European Synchrotron Radiation Facility (ESRF, Grenoble, France) at a wavelength of 0.3999 Å.

Petrography and mineral chemistry

Ultramafic material

In the peridotite layers of the FUB, the serpentinized olivine grains have characteristic mesh textures that either have relict olivine (FO_{92}) in the centres or are completely serpentinized. The mesh textures and XRD indicate that the serpentine phase is lizardite, with Mg# of 96. The detailed chemical compositions of the serpentine and olivine of representative samples are given in Table 1. In the serpentinized peridotite, bastites indicate completely serpentinized orthopyroxene grains and are marked by the high presence of magnetite and a lower concentration of Mg in the serpentine. Magnetite also appears at the boundaries of the serpentine meshes, as well as in between the meshes as bigger patches. Small μm sized awaruite grains are also present at the boundaries of the meshes. Chromite grains are common and have ferritchromite alteration rims. The presence of brucite is confirmed with XRD and interpreted in the BSE images as being located around the serpentine meshes due to the different contrast and the high Mg and Fe, and low Si concentration. Locally, brucite forms veins of a few μm across.

Table 1. *Representative electron microprobe data of main minerals in the ultramafic complex and in the tillite clasts*

	Ultramafic complex				Tillite clasts				
	Olivine	Serpentine un-weathered zone †	Serpentine blue weathered zone	Serpentine yellow weathered zone	Serpentine	Olivine	Quartz	K-feldspar	Muscovite
SiO_2	40.79	35.76	39.72	42.31	42.87	41.75	100.53	64.45	47.91
TiO_2	0.00	0.01	0.01	0.00	0.00	0.00	0.01	0.00	0.54
Al_2O_3	0.04	0.01	0.05	0.04	0.02	0.00	0.01	17.94	28.88
Cr_2O_3	0.00	0.02	0.01	0.04	0.01	0.06	0.00	0.04	0.00
FeO^T	7.84	3.17	3.00	3.31	2.09	7.09	0.06	0.05	5.23
MnO	0.11	0.10	0.09	0.03	0.11	0.11	0.01	0.00	0.02
MgO	51.60	45.02	41.99	39.90	41.12	51.97	0.01	0.01	1.55
CaO	0.02	0.01	0.03	0.07	0.05	0.02	0.00	0.00	0.00
Na_2O	0.00	0.00	0.01	0.00	0.01	0.00	0.00	0.24	0.04
K_2O	0.00	0.01	0.01	0.00	0.00	0.00	0.01	16.92	11.33
NiO	0.38	0.17	0.17	0.34	0.18	0.41	0.01	0.00	0.00
Total	100.77	84.27	85.07	86.03	86.45	101.41	100.66	99.67	95.50
Si	0.98	1.77	1.92	2.01	2.01	1.00	1.00	3.00	3.26
Ti	0.00	0.00	0.00	0.00	0.00	0.01	0.00	0.00	0.00
Al	0.00	0.00	0.00	0.00	0.00	0.00	0.00	0.99	2.32
Cr	0.00	0.00	0.00	0.00	0.00	0.00	0.00	0.00	0.00
Fe	0.16	0.13	0.12	0.13	0.08	0.14	0.00	0.00	0.30
Mn	0.00	0.00	0.00	0.00	0.00	0.00	0.00	0.00	0.00
Mg	1.86	3.32	3.02	2.82	2.87	1.85	0.00	0.00	0.16
Ca	0.00	0.00	0.00	0.00	0.00	0.00	0.00	0.00	0.00
Na	0.00	0.00	0.00	0.00	0.00	0.00	0.00	0.02	0.01
K	0.00	0.00	0.00	0.00	0.00	0.00	0.00	1.01	0.98
Ni	0.01	0.01	0.01	0.01	0.01	0.01	0.00	0.00	0.00
Total cation	3.00	5.22	5.07	4.97	4.98	3.00	1.00	5.02	7.02
O p.f.u.	4.00	7.00	7.00	7.00	7.00	4.00	2.00	8.00	11.00
Mg#*	0.92	0.96	0.96	0.96	0.97	0.93	-	-	-

†The serpentine from the un-weathered zone is a mix of serpentine and brucite

*Mg# = Mg/(Mg+Fe)

Weathering of ultramafic material

The ultramafic body is weathered both in physical and chemical ways as outlined by Ulven *et al*. (2017). Multiple m-scale fractures are present (Fig. 3a), and weathering rinds can be observed at the outer 1 to 2 cm of the whole ultramafic complex (Fig. 3b). The weathering rinds consist of an inner blueish weathered zone directly around the unweathered peridotite and an outer yellowish weathered zone at the outermost boundary that is in contact with the atmosphere. While the outer weathering front is rather diffuse, the inner weathering front is sharp and clearly visible with optical microscopy due to the colour change from light

green to dark brown in plane polarized light. In terms of mineralogical composition, the weathered zone is very similar to the unweathered serpentinized peridotite, with mesh textured serpentine and relict olivine (FO_{92}) of the same composition. However, chemical analysis shows that the serpentine areas in the weathered zone are depleted in Mg and enriched in Si compared to the serpentine in the unweathered peridotite (Table 1). This is enhanced towards the outer part of the alteration rim. In contrast to the unweathered part, XRD does not show any signs of brucite in the weathered zone (Fig. 3d). Whole rock analysis also indicates that the weathered zone is depleted in Mg compared to the unweathered part. This is additionally illustrated in element maps across the weathering front, which show that the areas in between the meshes are depleted in Mg and slightly enriched in Fe on the weathered side (Fig. 3c). In addition, the weathered zone is more porous then the unweathered zone and shows dissolution textures. Pyroaurite is also present in the weathered zone.

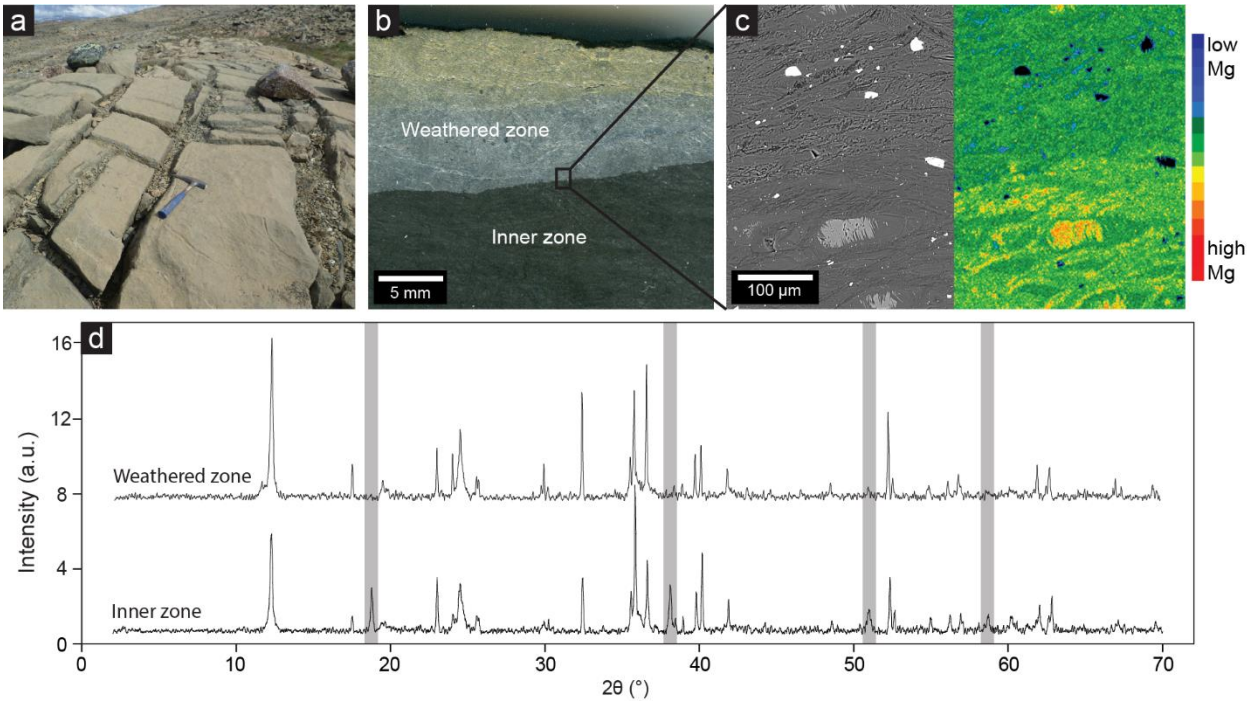

***Fig. 3**. Weathering of the peridotite and the dissolution of brucite. (**a**) Field picture showing the fractures in the ultramafic rocks where the weathering penetrates tens of cm into the rocks. (**b**) Sample of serpentinized peridotite cut perpendicular to the weathering rind. The weathering rind consists of an outer yellow and an inner blueish zone. (**c**) BSE image (left) and Mg map (right) across the weathering front illustrating the depletion of Mg in the weathered zone. (**d**) XRD patterns of the weathered zone and the unweathered inner zone of the serpentinized peridotite, with the grey boxes indicating the peaks of brucite, which lack in the weathered zone. The other peaks correspond to lizardite, olivine and magnetite.*

Tillite

The cemented tillite contains fragments of the underlying ultramafic complex and from the glacial deposits (Fig. 4). These clasts are angular and unsorted, with a size ranging from <1 μm to 10 cm, and are either single phase grains enclosed in the matrix (Fig. 4a), or rock fragments which can consist of multiple phases and which are often infiltrated with cement (Fig. 4b). The ultramafic clasts are serpentinite fragments, which locally contain olivine and magnetite. The texture and composition of the olivine and serpentine in the clasts indicate that the material is derived from the FUB. Fragments of andradite with similar composition as the veins in the lherzolite layers confirm the FUB source (Plümper *et al*. 2014). Most ultramafic clasts are similar to the serpentinite from the outer Mg-depleted weathered zone of the FUB (Table 1). However, some clasts show the weathering front and contain brucite (Fig. 4b). It is unclear if this weathering occurred *in situ* or before the cementation. The felsic clasts consist mainly of quartz, K-feldspar and muscovite, which compositions are listed in Table 1. Furthermore, minor amounts of albite and illite and occasionally rutile, iron-oxide, titanite, ilmenite, apatite, epidote and zircon can be found. The larger rock fragments (>1 mm) in the tillite usually consist of a combination of quartz, K-feldspar and muscovite. Aggregates of quartz grains are also common and undulate extinction, subgrains and grain boundary migration indicate crystal-plastic deformation and dynamic recrystallization of the quartz. The straining most likely originated within the original host rock or was partly induced during the glaciation.

The rock fragments in the tillite are typically infiltrated with cement along the grain boundaries (Fig. 5a). As a result, the clasts are disintegrated into smaller fragments separated by M-S-H cement (Fig. 5b). The strained quartz grains develop very remarkable textures as a result of dissolution and precipitation of cement. This leads to honeycomb textured cement that is widely present in the cemented rocks (Figs. 6a–b). M-S-H cement is present in quartz aggregates along (sub)grain boundaries or within fractures which disintegrates grains of a few 100 μm into smaller single quartz grains of a few tens of μm (Fig. 6c), or of only a few μm (Fig. 6d). The grains that are partly or completely dissolved leave behind pore space in the shape of a quartz grain in the cement, creating a honeycomb-like shape (Figs. 6e–f). Frequently, the honeycombs are (partly) filled with cement and the quartz grains are close to completely replaced by cement (Fig. 6g). Sometimes, the outline of the quartz grains is still visible in the cement (Fig. 6h). The quartz aggregates thus have different appearances within the tillite as can be observed in Figs. 6a–h: (1) strained and/or recrystallized; (2) with cement in between (sub)grain boundaries and fractures; (3) with cement in between (sub)grain boundaries and (partly) dissolved quartz grains; or (4) completely replaced by cement. Moreover, combinations of these textures can be found within one aggregate as dissolution can be restricted to the

outer part. The disintegrated felsic fragments and quartz aggregates show that they once formed one fragment of which the outline is still visible (Figs. 5a–b, 6a–b).

The majority of the feldspar grains are K-feldspar and the rest is albite, commonly antipertitic. Many feldspar grains are partly dissolved and replaced by M-S-H cement, although in contrast with quartz it only appears on the outer boundaries, which results in remarkable shaped grains (Fig. 7). At the places where the K-feldspar is dissolved, the cement often contains tiny crystalline grains rich in Al and K (illite). Illite replaces the K-feldspar in the felsic rock fragments and single needles of illite of only a few µm across are common in the cement and might be weathering products of K-feldspar.

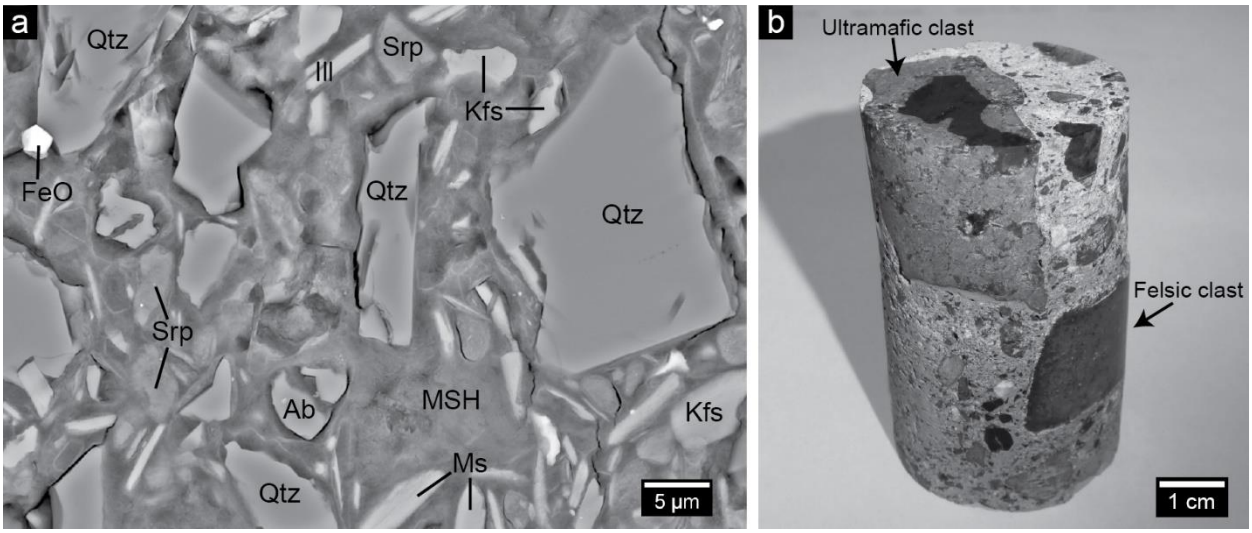

Fig. 4*. Cemented tillite from the Feragen field area. (**a**) BSE image showing µm-scale single grained clasts with irregular and angular grain boundaries enclosed in the M-S-H matrix. The most common clasts are quartz (Qtz), K-feldspar (Kfs), albite (Ab), serpentine (Srp), Muscovite (Ms), illite (Ill) and iron oxides (FeO). (**b**) Drill core sample with cm-scale felsic and ultramafic clasts, with the latter being a partly serpentinized dunite with a weathering rind.*

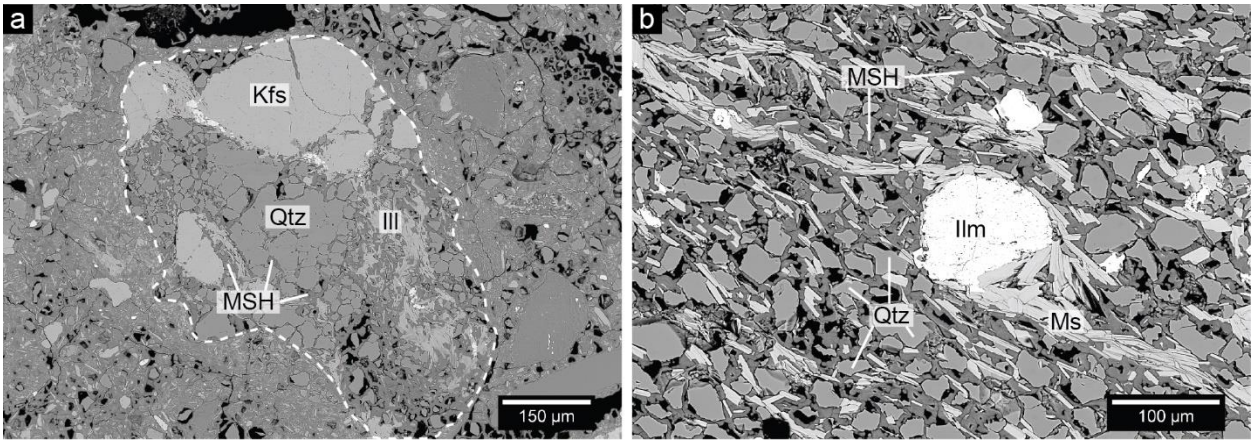

Fig. 5*. BSE images showing the infiltration of M-S-H cement into felsic rock fragments within the tillite. (**a**) A disintegrated rock fragment consisting of quartz (Qtz), K-feldspar (Kfs) and illite (Ill), indicated by the dashed line, with M-S-H cement (MSH) present in between the grains. (**b**) A mm-sized fragment of quartz with ilmenite (Ilm) and muscovite (Ms) is disintegrated into single quartz grains and the space in between is filled with M-S-H cement.*

Fig. 6 (next page)*. BSE images from the tillite showing quartz (Qtz) dissolution and replacement by M-S-H cement (MSH). (**a**) The outline (indicated by the dashed line) of a quartz fragment which is partly replaced by cement with a honeycomb texture. (**b**) Another relict of a quartz grain which is almost completely replaced by cement with a honeycomb texture. Note that some of the honeycomb cells contain quartz grains in their centres. (**c**) A quartz grain that is broken up into smaller grains along its outer boundary. Cement is formed in between the smaller grains. (**d**) A quartz grain that is partly disintegrated and infiltrated by cement. (**e**) Cement shaped as honeycombs in a fracture within a quartz grain. (**f**) Honeycombs of cement with some leftovers of quartz, the empty honeycombs have the shape of the former quartz grains. (**g**) A quartz grain (indicated by the dashed line) which is almost completely replaced by cement. (**h**) The cement shows bright lines that are the outlines of the former quartz grains.*

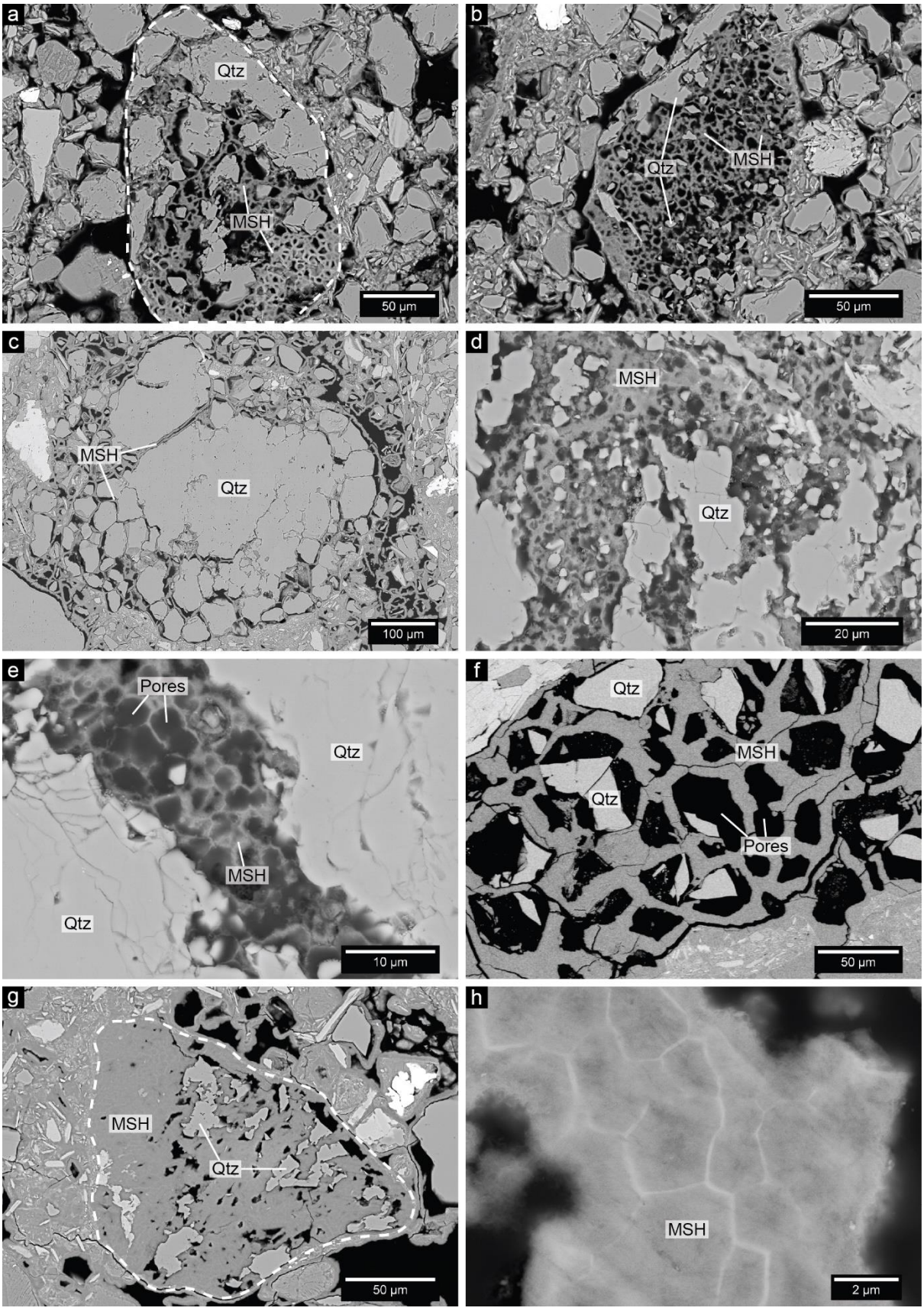
a
Qtz
MSH
50 µm
b
Qtz
MSH
50 µm
c
MSH
Qtz
100 µm
d
MSH
Qtz
20 µm
e
Pores
Qtz
MSH
Qtz
10 µm
f
Qtz
MSH
Qtz
Pores
50 µm
g
MSH
Qtz
50 µm
h
MSH
2 µm

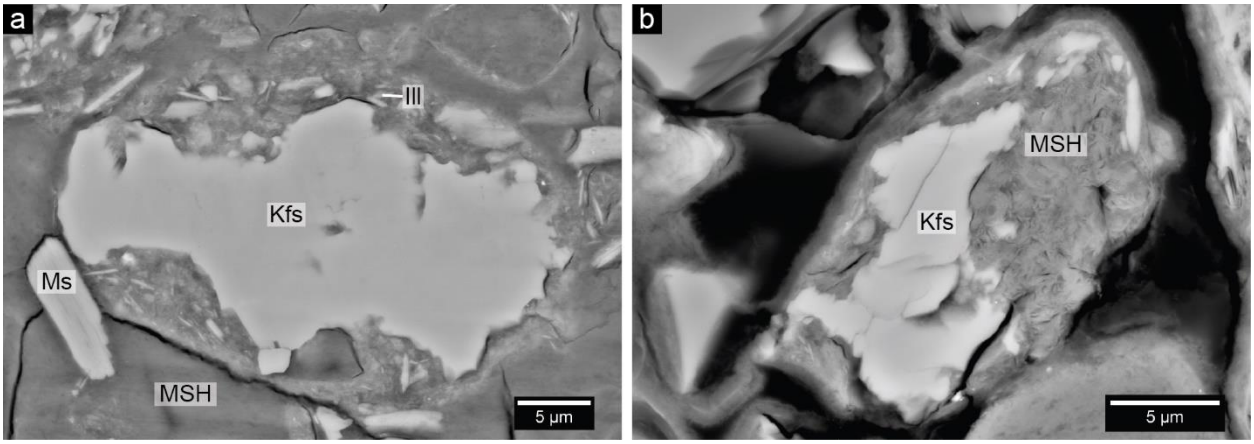

Fig. 7*. BSE images of K-feldspar (Kfs) in the tillite which is surrounded by M-S-H cement (MSH). (**a**) K-feldspar grain which is replaced by cement along its boundary. The original outline of the feldspar grain is visible due to colour difference in the cement and by the presence of tiny illite (Ill) grains within the cement that replaced the feldspar. Muscovite (Ms) is also present. (**b**) A K-feldspar grain partly replaced by M-S-H cement.*

Cement

Microprobe analysis of the cement reveals it is a magnesium silicate hydrate phase. Detailed chemical data of the cement from a number of samples is given in Table 2. The calculated number of cations indicate a structural formula of $Si_8Mg_8O_{20}(OH)_8 \cdot 6H_2O$. The amount of H_2O is obtained by subtracting the total of the microprobe analyses from a total of 100. This structural formula does not correspond to any known mineral, but points to a phyllosilicate comparable to serpentine ($Mg_3Si_2O_5[OH]_4$), talc ($Mg_3Si_4O_{10}[OH]_2$) and sepiolite ($Mg_4Si_6O_{15}[OH]_2 \cdot 6H_2O$). The cement is homogeneous in composition within the samples and there is also little variation between samples as can be observed from Table 2. The Mg/Si ratio is on average 1.00 and varies from 0.86 to 1.21, although the majority of the measurements indicate a ratio between 0.9 and 1.1. There is no correlation between the composition and the setting in which the cement is found. Fig. 8 shows the results of all the compositional analyses of the cement from which the homogeneity can be observed. Cement adjacent to K-feldspar contains more Al and less Mg compared to the regular M-S-H cement. The amount of Al_2O_3 varies but is typically around 2 wt%, although 20 wt% has also been measured.

Powder X-ray diffraction spectra of the cemented rock include many peaks corresponding to the wide variety of clasts. As can be observed in Fig. 9, two bulges occur at 2θ of 36° and 60°, which match with M-S-H cement of a Mg/Si ratio of 1 that has been produced in multiple cement research studies (Brew & Glasser 2005; Li *et al.* 2014; Zhang *et al.* 2014; Roosz *et al.* 2015). Peaks of this shape generally indicate

a nanocrystalline phase, meaning poorly crystalline but not amorphous. In the case of phyllosilicate minerals, this typically means that the crystal layers have a stacking disorder and are thus turbostratic. This is a common feature of clay minerals that formed under low temperature surface conditions (Meunier 2006). The combination of the peaks at 36° and 60°, corresponding to d-spacings of 2.5 Å and 1.5 Å, are typical for trioctrahedral phyllosilicates like serpentine, sepiolite, talc and other Mg-rich clay minerals like stevensite and kerolite. The peak at 36° corresponds to the 20*l* and 30*l* reflections which occur as one low and broad peak due to the turbostratism. The peak at 60° is the 060 reflection which indicates the phase is trioctahedral, which fits with the obtained structural formula. At low 2θ, another broad peak is present in the natural cement. This is the 001 reflection, which for phyllosilicates means it is the distance between the parallel crystal layers. In this case, the peak corresponds to a d-spacing of 15.5 Å, which fits with stevensite, a Mg-smectite mineral. However, the smaller broad peak present at 72° (d-spacing of 1.3 Å) is typical for kerolite, which basically is nanocrystalline stacking-disordered talc. Stevensite and kerolite are both known to precipitate from solutions under high pH (>9) conditions at low temperatures (Tosca & Masterson 2014). As the composition points out as well as the XRD data, the cementing phase is a mixture of two or more Mg-rich phyllosilicates related to Mg-rich clay minerals and/or serpentine.

Table 2. *Representative electron microprobe data of the cement in different samples*

	FER11-15	STE1-15	FER2-15	FER17-15B	FER16-2B	FER16-9B	Average
SiO_2	47.19	43.72	50.28	51.42	48.18	50.81	48.60
TiO_2	0.00	0.00	0.03	0.00	0.00	0.02	0.01
Al_2O_3	0.07	0.73	0.07	0.27	0.56	0.51	0.37
Cr_2O_3	0.01	0.01	0.03	0.02	0.02	0.02	0.02
FeO^T	0.01	1.46	0.03	0.01	0.18	0.08	0.30
MnO	0.00	0.07	0.00	0.01	0.04	0.00	0.04
MgO	31.70	33.72	34.68	30.88	31.55	32.93	32.58
CaO	0.12	0.22	0.16	0.53	0.20	0.38	0.27
Na_2O	0.00	0.00	0.00	0.00	0.00	0.02	0.00
K_2O	0.01	0.12	0.02	0.05	0.04	0.09	0.05
NiO	0.04	0.12	0.01	0.00	0.05	0.06	0.05
Total	79.13	80.17	85.31	83.20	80.83	84.90	82.28
Si	8.02	7.43	8.55	8.74	7.70	8.12	8.10
Ti	0.00	0.00	0.00	0.00	0.01	0.01	0.00
Al	0.01	0.15	0.01	0.06	0.10	0.10	0.07
Cr	0.00	0.00	0.00	0.00	0.00	0.00	0.00
Fe	0.00	0.21	0.00	0.00	0.02	0.01	0.04
Mn	0.00	0.01	0.00	0.00	0.01	0.00	0.00
Mg	8.03	8.55	8.79	7.83	7.52	7.85	8.09
Ca	0.02	0.04	0.03	0.10	0.03	0.06	0.05
Na	0.00	0.00	0.00	0.00	0.00	0.00	0.00
K	0.00	0.03	0.00	0.01	0.01	0.02	0.01
Ni	0.01	0.02	0.00	0.00	0.01	0.00	0.00
Total cation	16.10	16.43	17.40	16.74	15.41	16.18	16.38
O p.f.u.	24.00	24.00	24.00	24.00	24.00	24.00	24.00
Mg/Si	1.00	1.15	1.03	0.90	0.98	0.97	1.00

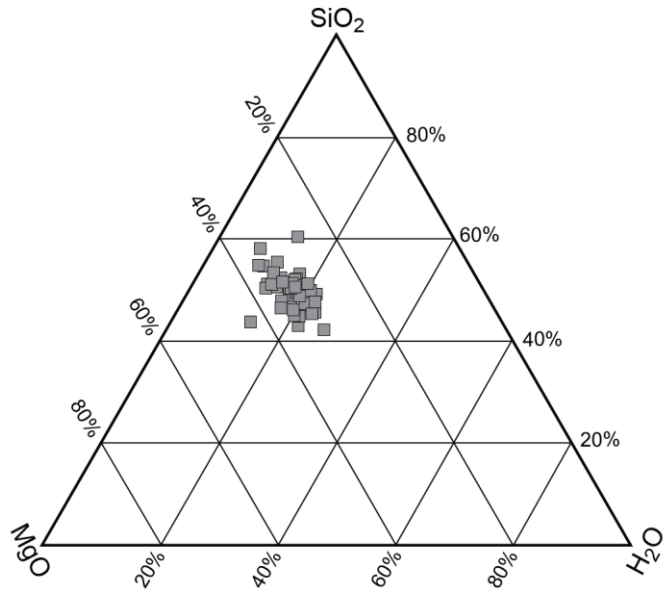

Fig. 8*. Ternary diagram with the composition of the cement from all analysed samples, with SiO_2, MgO and H_2O given in wt%. Errors are within the size of the symbols.*

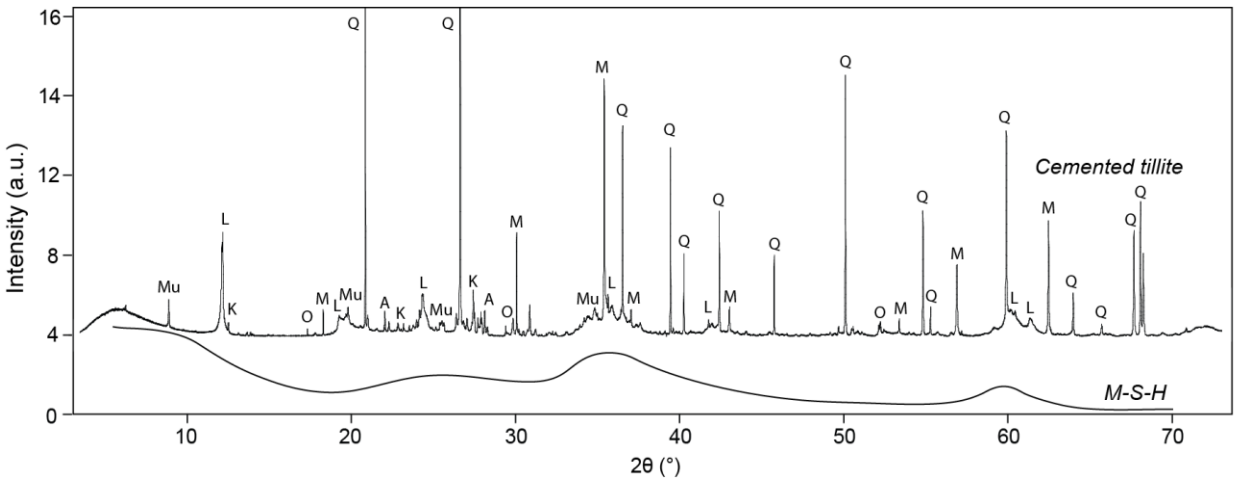

Fig. 9. *X-ray diffraction spectrum (CuKα) of the cemented tillite (top spectrum), with indications of the minerals that are present as the main clasts: muscovite (Mu), lizardite (L), K-feldspar (K), olivine (O), magnetite (M), quartz (Q) and albite (A). The low and broad peaks at 15°, 36°, 60° and 72° correspond to the cementing phase and indicate a mixture of two or more Mg-rich phyllosilicates related to Mg-rich clay minerals and/or serpentine. The two peaks at 36° and 60° match in position and shape with the spectrum of man-made M-S-H from Zhang et al. (2016) (bottom spectrum).*

Discussion

Cementation process

Multiple processes are preceding the cementation of tillite and are all of importance for the formation of the final cement; serpentinization, glacial processes, weathering, dissolution and evaporation. Brucite forms during serpentinization of olivine according to the reaction (written for the Mg endmembers):

$$2Mg_2SiO_4 + 3H_2O \rightarrow Mg_3Si_2O_5(OH)_4 + Mg(OH)_2 \quad (1)$$

The reaction products consist of brucite and serpentine in an equimolar ratio. In nature, brucite is usually present as intergrowth in the serpentine mesh rims and is typically less abundant than serpentine since the Fe present in olivine and the presence of pyroxene reduce the amount of brucite (Bach *et al.* 2006; Frost & Beard 2007). The amount of brucite present in the unweathered inner part of the ultramafic rock at Feragen is up to 10 wt%. It is most likely that the hydration process that led to brucite formation took place at the ocean floor before exhumation. At its current position at the Earth's surface, the ultramafic complex is far out of equilibrium and will undergo rapid weathering when in contact with air and water, as is also obvious from Goldish dissolution series (Goldich 1938). While the weathering of peridotite in humid and tropical areas where high rainfall and high temperatures enhance the kinetics has been well studied (Beauvais *et al.* 2007; Schopka *et al.* 2011; Ratié *et al.* 2015; Genthon *et al.* 2017), the FUB is based in a cold and relatively dry climate and less is known about the weathering rate under such subarctic conditions. The yearly freezing and thawing will nevertheless result in physical weathering and the rainfall and yearly snow melting will lead to chemical weathering. The combination of physical and chemical weathering has important implications, since the porosity originating from dissolution reactions can initiate large scale fractures due to the freeze-thaw cycle. Fracturing will subsequently lead to enhanced fluid transport and the creation of new surface area that will promote dissolution and precipitation processes, creating a positive feedback loop (Ulven *et al*. 2017). The 2 to 3 cm thick alteration rim that is present around the whole ultramafic complex is depleted in Mg due to the dissolution of brucite, as evident from XRD, whole rock analysis, chemical mapping and microprobe analysis. The dissolution of brucite in general leads to the release of Mg^{2+} and the increase in pH:

$$Mg(OH)_2 \rightarrow Mg^{2+} + 2OH^- \quad (2)$$

Dissolution of brucite in serpentinites has been observed in nature (Mumpton & Thompson 1966; Beinlich & Austrheim 2012) and is also expected based on the fast dissolution rate obtained in experimental studies (Pokrovsky & Schott 2004; Hövelmann *et al.* 2012), which is about 4 to 5 orders of magnitude higher than the dissolution rate of serpentine at surface conditions (Bales & Morgan 1985; Daval *et al.* 2013). The water at the surface and in mines at the FUB has a pH between 9 and 10 and a Mg^{2+} concentration between 13 and 89 mg/l (versus 0.02 mg/l in the rainwater), as measured by Beinlich and Austrheim (2012). The dissolution of brucite hence has to be an ongoing fast process that takes place on a time scale of days by the infiltration of rainwater into the ultramafic rocks. This also indicates that the dissolved Mg is transported within the surface water and groundwater. In the same study, a Si (as SiO_2) concentration between 1 and 12 mg/l has been measured in the area. The presence of Si in water is also indicated by the occurrence of a coating of diatoms in small nearby streams, which are a type phytoplankton known for their external cell wall of silica.

The glaciation resulted in the deposition and mixing of felsic and ultramafic material on top of the ultramafic rocks and is therefore of significant importance in the cementation process as this brought a high quantity of Si towards the Mg-releasing ultramafic rocks. Consequently, the exceptional mixture of fractured serpentinized ultramafic rocks and felsic till occurs. Although glaciers were widespread in the Northern Hemisphere during the last glaciation, preservation of quartz-rich till at the surface in combination with an ultramafic complex is rather uncommon, which is perhaps one of the reasons M-S-H cement has not been found at other places in nature.

The appearance of the partly dissolved quartz surrounded by the M-S-H cement indicates that the quartz must be dissolved *in situ* during or after the cementation process and cannot be a remnant of earlier processes. This is for example evident from the honeycomb shaped cement which, based on the shape and the occasional presence of quartz inside the honeycombs, originally formed around quartz grains which are dissolved afterwards (Figs. 6a–f). Furthermore, disintegrated felsic fragments that are infiltrated with cement indicate the same history since their shape (Fig. 5a) and internal lineation (Fig. 5b) would not have been preserved if disintegration occurred before cementation. The infiltration of M-S-H cement starts along (sub)grain boundaries or fractures in combination with dissolution and is breaking up the quartz to form the textures visible in Figs. 6c–d. Where cement is replacing quartz completely as shown in Fig. 6g, the outline of the original quartz grains is preserved and represents cement filled honeycombs (Fig. 6h). This indicates that quartz dissolves after being surrounded by cement and that, eventually, cement replaces the quartz completely (Fig. 10). The *in situ* occurrence means that the dissolution happens under sub-arctic surface conditions in less than 100 years, since it is unlikely that the cementation of the mine walls, and thus the

quartz dissolution, started during the mining activities. It is accepted that quartz weathers very slowly due to its high stability and that the lifetime of 1 mm of quartz is 34 million years at 25 °C and a pH of 5 (Lasaga 1984). Nevertheless, the size of the honeycombs indicates that at least 10 μm of quartz has been dissolved in maximum 100 years, which is 8500 times faster.

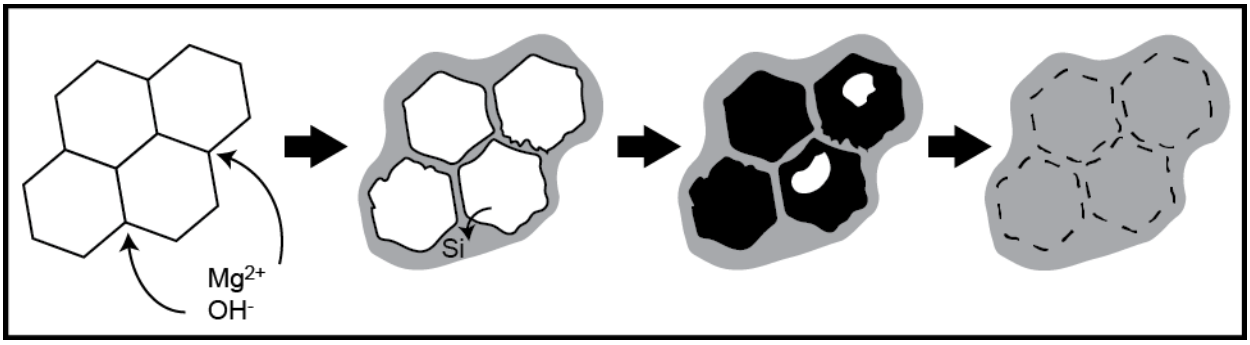

Fig. 10*. Schematic illustration of the dissolution of quartz and the formation of honeycomb textured cement. Mg-rich high pH fluid reacts at the grain boundaries of quartz aggregates, where dissolution starts and M-S-H cement will be precipitated. After being surrounded by M-S-H cement, the quartz grains dissolve completely and subsequently might get filled with cement.*

However, experiments have shown that the dissolution rate of quartz increases rapidly with increasing pH. When the pH rises above the pK_a for silicic acid, the resulting compound when dissolving quartz, quartz becomes orders of magnitudes more soluble. The solubility continues to increase with increasing pH. For this reason, the log rate for quartz dissolution at a temperature of 25 °C and a pH of 10 is around -11.5 mol m^{-2} s^{-1}, which is one order of magnitude higher than at a pH of 5 (Brady & Walther 1990; House & Orr 1992). This is however still much slower than what our observations in the mine walls indicate. But, if the solutions that flow through this system get saturated with brucite the pH can rise above 10, creating a far-from-equilibrium situation that drives the dissolution of quartz. Recent studies have calculated rate law equations for quartz dissolution that match the experimental data (Bickmore *et al.* 2008; Rimstidt 2015), in which the influence of temperature, hydrogen ion activity and sodium concentration on the dissolution rate is emphasized. Especially the influence of sodium, potassium and other alkaline cations might have an underestimated effect on the dissolution of quartz in nature, since most experimental studies use pure water or water with a low ionic strength, which is not representative for pore water in rocks that is enriched in cations due to weathering and evaporation. The study of Rimstidt (2015) shows that in a sodium concentration equivalent to seawater the dissolution is at least 2 orders of magnitudes faster than in pure water, while not even taking into account the presence of other cations like K, Ca and Mg, which are all confirmed to catalyse dissolution of quartz (Dove & Nix 1997). The release of K and Na from K-feldspar

and albite during dissolution in the presence of the high pH fluid could thus enhance this process. In the FUB field area, the high Mg concentration and high pH resulting from the weathering of brucite and the high ionic strength as a result of evaporation at the surface are thus known to enhance the dissolution of quartz, although no experimental studies have used the combination of low temperatures, high ionic strength and high pH and hence no expected rate can be given. Extrapolating the known rate equations of quartz dissolution might be ambitious since the exact fluid composition at the interface of the fluid and the quartz is unknown. Furthermore, deformation of minerals tends to enhance the dissolution rate (Schott *et al.* 1989; Tromans & Meech 2001), and since the quartz shows signs of straining this might be applicable for this case. Also, the occurrence of quartz as aggregates of multiple small grains means a high surface area and numerous grain and subgrain boundaries where fluids can more easily penetrate. The difference in grain orientations within the quartz aggregates indicates the presence of grain boundaries before cement has been infiltrated and is most likely a remnant of an early deformation phase.

Feldspar shows similarities with quartz as multiple grains are dissolved at the grain boundaries where it is replaced by M-S-H cement which is slightly enriched in Al. This shows that the dissolution of the minerals is closely related to the precipitation of cement and thus a coupled dissolution-precipitation process is occurring (Putnis 2002). The dissolution of K-feldspar is limited to the outer boundaries of the grains, probably because of the lack of internal (sub)grain boundaries. The fluid that reacts with the quartz and feldspar is enriched in Mg, which, as discussed above, is transported within the ground and surface water. Flow systems played an important role as the Mg-rich and high pH fluid is transported towards the till. This explains the occurrence of the cement at flat areas which are topographically lower than the ultramafic body, as that is the place where the fluids will flow towards and accumulate. In addition, the cold and dry air will lead to evaporation and consequently fluid saturation. Hence, cement will be precipitated at the surface. It should also be noted that the precipitation in the field area is relatively low, meaning there is little outflow of water, except when the snow melts in spring. This gives the fluids time to saturate and react with the till. The cement that has been formed behind boulders (Fig. 2d) can be explained by this principle; groundwater is pushed upwards behind the boulder and since the surface is flat, water will become trapped and saturate over time (Fig. 11a). The cement layers that can be found in patterned ground (Fig. 2c) are likely formed due to the same principle; water is accumulating due to capillary effects related to the formation of ice lenses in winter which melt in spring (Fig. 11b). At the walls of the mine entrances (Fig. 2a), the airflow through the mineshaft might enhance evaporation so that thicker layers of cement can form than at other places at the surface (Fig. 11c). The construction of the mines inside the ultramafic rocks would have enhanced fracturing allowing rain and groundwater fluids to have more contact with the serpentinized rocks. How boulders of cemented tillite of more than 0.5 m across can form is not clear (Fig. 2b). However, the

locations where they are found always show soil movements like terraces and cracks in the soil, which are all signs of frost heave and thus water accumulation. At all locations, high pH fluids enriched in Mg, as induced by weathering of the ultramafic material, lead to the dissolution of quartz and its subsequent replacement by cement (Fig. 10).

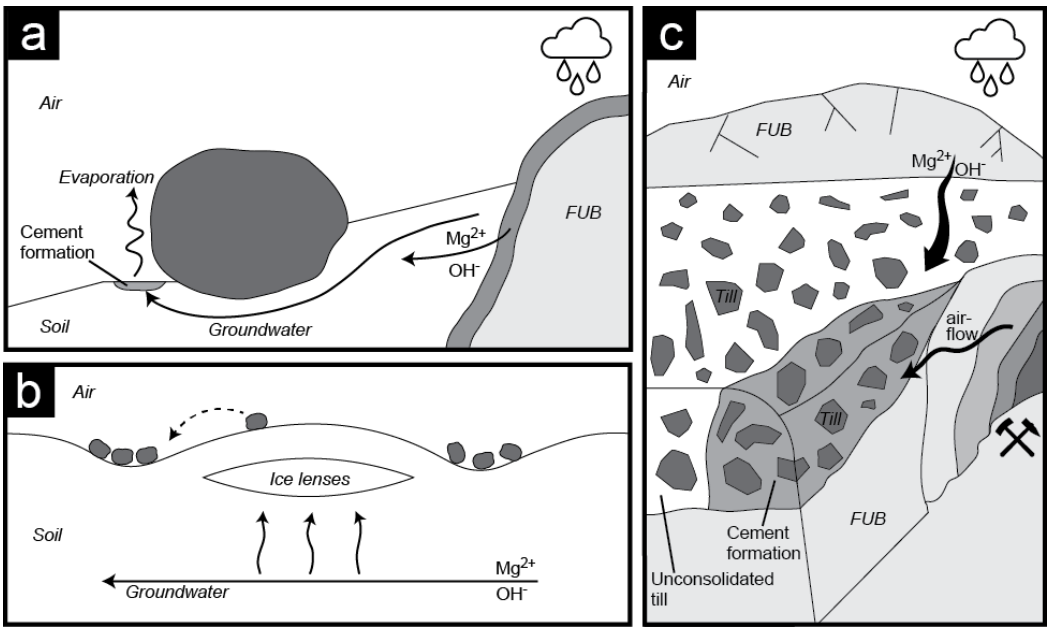

***Fig. 11**. Sketches illustrating the formation of M-S-H cement in three settings. In all three settings, cement forms where high pH and Mg-rich water accumulates and can evaporate to increase the ionic strength so that quartz dissolution and cement precipitation is possible. (**a**) Cement formed at the downhill side of a boulder where the Mg-rich high pH groundwater, which originates from the weathered zone of the ultramafic complex (FUB), moves upwards and evaporates. Cement is precipitated from the resulting supersaturated fluids. (**b**) Formation of polygonal soil patterns by frost heave. The frost heave sorts sediments by size and leads to the accumulation of water due to the capillary action that feeds the ice lenses. When the ice melts in spring and the water evaporates, cement forms in the centres of the polygons. (**c**) A cross-section through one side of the wall in front of a mine shaft, with the fractured ultramafic complex (FUB) in the background that provides Mg-rich and high pH fluids. Thicker layers of cemented till (approximately 30 cm) occur at the wall due to enhanced evaporation by the airflow through the tunnel, which makes the fluids supersaturated so that quartz will dissolve and the cement can form. Behind the cemented part of the wall, the till is unconsolidated.*

The arguments above point to a process by which dissolved brucite and quartz form a hydrous magnesium silica phase which cements the till. Experimental work has shown the formation of M-S-H cement with a Mg/Si ratio of 1 from a reaction with MgO and silica fume (amorphous silica), where the MgO first hydrates to brucite and then reacts with the silica (Zhang *et al.*, 2014). M-S-H cement has also been produced from a reaction with silicic acid and brucite (Temuujin *et al.* 1998). The formation of the cementing phase from brucite and quartz as expected at Feragen could occur via the following reaction:

$$8Mg(OH)_2 + 8SiO_2 + 2H_2O \rightarrow Mg_8Si_8O_{20}(OH)_8 \cdot 6H_2O \quad (3)$$

The M-S-H phase is most likely a mixture of two or more nanocrystalline phyllosilicates related to serpentine and/or Mg-rich clay minerals like stevensite and kerolite. Studies on the structure of man-made M-S-H cement claimed that the phase is turbostratic with a short-range stacking order (Roosz *et al.* 2015), which fits with the XRD spectra of the natural M-S-H cement obtained in this study. However, it should be noted that the exact nature of the poorly crystalline phyllosilicates of man-made M-S-H cement is not well understood. Also, comparing our data to natural Mg-rich clay and serpentine minerals give unambiguous results. Nevertheless, XRD data combined with compositional data does show that the cement consists of turbostratic Mg-rich phyllosilicates formed from supersaturated solutions under high pH and low temperature conditions, and hence showing similarities to natural Mg-silicate minerals (Tosca & Masterson 2014).

The Mg-rich clay minerals kerolite, sepiolite, stevensite and talc are also hydrous magnesium phyllosilicates that form from reactions taking place under Earth surface conditions. These Mg-silicates are known to form directly from water when the solution is supersaturated with respect to the mineral phase, since this creates a thermodynamic driving force (Tosca 2015). The high supersaturation that is required for their precipitation can be created by rapid changes in the water chemistry, for example by evaporation, which can drive the system beyond critical supersaturation. This is evident from well-studied alkaline lake systems in which Mg-silicates precipitate due to evaporation, since this leads to highly saturated and alkaline conditions (Wright & Barnett 2015). Lake Chad is an example of a lake system is which this has been reported (Gac et al. 1977; Darragi & Tardy 1987), as well as the Pantanal wetlands in Brazil (Furquim et al 2008). Supported by several experimental studies (Tosca and Masterson 2014), it is thus known that in highly alkaline settings evaporation generally leads to the homogeneous nucleation of Mg-silicates from solutions. Tosca and Masterson (2014) experimentally investigated what controls the crystallization of such Mg-silicates from solution, showing that the pH, salinity and the Mg/Si ratio influences the products that form and thus defines the type of Mg-rich clay mineral. It also indicates the high pH threshold that is

required for the precipitation of Mg-silicates and at the same time for the avoidance of amorphous silica precipitation. The formation of Mg-silicates at the Feragen ultramafic complex is governed by different mechanisms than the Mg-silicates discussed above. However, it does show that our hypothesised formation process, which states that M-S-H forms in an alkaline environment by evaporation followed by supersaturation and precipitation, is indeed an established way of Mg-silicate formation. The natural Mg-rich clay mineral systems also indicate that the unusual high pH conditions occurring at the Feragen area are within the threshold of low temperature Mg-silicate nucleation and provide chemical conditions suitable for the formation of different Mg-silicate phases. In natural examples of clay mineral formation at the surface, clays are usually not well-crystallized and have a size in the order of nm because nucleation is energetically favourable above crystal growth (Meunier 2006). This is in agreement with the M-S-H at the Feragen area and the M-S-H of other experimental studies, where the resulting cement is always nanocrystalline.

Green cement

Man-made M-S-H cement shows remarkable similarities with the natural M-S-H cement. According to Zhang *et al*. (2014), their M-S-H has a formula of $Si_8Mg_8O_{20}(OH)_8 \cdot 12H_2O$, which only differs in the amount of water compared to the natural M-S-H cement studied. Furthermore, X-ray diffraction shows that the atomic structure is similar as can be observed in Fig. 9. The use of various types of industrial magnesium-based cement is limited to specialist applications, and M-S-H cement is not commercially used at present. This is mainly caused by the lack of feasible sources of reactive silica and missing information on fundamental issues as the long-term durability, the structure of the phase, the mechanical properties and the influence of chemical conditions on its formation. Moreover, the implementation of more environmentally friendly cement in the construction sector in general has proven to be challenging due to a variety of reasons as outlined by Dewald & Achternbosch (2016). It is nevertheless unsure if M-S-H would be applicable as a building cement, but it does have potential to be used in the future in nuclear and chemical waste encapsulation as shown by Zhang *et al*. (2012). Its low alkalinity in comparison with Portland cement is advantageous in encapsulation of metallic aluminium waste from nuclear industry. One of the main breaking points is, as mentioned, the source of fast reacting silica. In the natural M-S-H formation process at Feragen, quartz dissolution is also the rate-limiting factor. Although the dissolution rate is many times faster under the conditions occurring at Feragen than under normal natural conditions, it is still too slow for industrial applications. Nevertheless, since multiple processes enhance the dissolution rate with orders of magnitude, it should not be ruled out that the rate can be increased to a feasible level when the ideal conditions are known. Straining of the quartz, high ionic strength, the presence of catalytic cations and a

high pH are all conditions that enhance the dissolution rate of quartz at Feragen but of which the optimum combination remains unknown. Further research about the reactivity of quartz under these conditions could lead to the optimization of quartz dissolution. It should also be taken into account that the temperature at Feragen is far from ideal and no dissolution occurs during half of the year when the ground is frozen. The presence of Si in the surface water in the area possibly indicates the dissolution of other present silicate minerals like serpentine and olivine. Part of the silica that forms M-S-H could therefore originate from these minerals. Also, diatoms form because of the presence of silica, which they need to form their silica cells. In an experimental study, Brehm *et al.* (2005) reported how biofilms of diatoms can create local pH shifts from 3.4 to higher than 9 and that the quartz which was covered with the biofilm was locally perforated to a depth of more than 4 mm. No remains of diatoms were found in the cemented rocks so it is unlikely they are responsible for the *in situ* quartz dissolution, but they might provide additional silica in the regional percolating fluids. Furthermore, the dissolution of the silica cells of dead diatoms is faster than quartz since it is not a crystalline phase and could therefore also be an additional source of silica. This study shows that quartz dissolution and subsequent M-S-H cement formation can be very efficient under specific conditions in nature, and therefore hopefully paves a way for more detailed studies on optimized conditions for this process so that the potential of M-S-H cement will be exploited as much as possible.

Conclusion

Magnesium silicate hydrate cement forms in the unique conditions of the Feragen ultramafic complex, where weathering of serpentinized rocks occurs in the presence of quartz-rich felsic glacial deposits. The cement is a nanocrystalline phyllosilicate phase that forms from the reaction of dissolved brucite with quartz and leads to the cementation of tillite. The exceptional high dissolution rate of quartz, which is enhanced by the presence of high pH and cation-rich fluids that are the result of weathering and evaporation, makes it possible for the cement to form on the time scale of decades in subglacial conditions. This is the first time the formation of natural M-S-H has been described but it shows remarkable similarities with man-made M-S-H which is currently of interest as it has a potential as CO_2-neutral or nuclear waste encapsulating cement. However, many details and a feasible silica source are lacking which hinders a large scale industrial application. This study might provide additional insights useful for tackling these issues.

Acknowledgements and funding

We thank Ole Ivar Ulven for his assistance in the field, Boaz Pokroy for the synchrotron XRD analysis and Dag Kristian Dysthe for the helpful discussions. We are grateful to Depan Hu for making his master thesis

589 available to us and Arianne Petley-Ragan is thanked for her constructive comments on the manuscript. We
590 thank Benjamin Tutolo and an anonymous reviewer for their insightful and constructive reviews. This
591 project has received funding from the European Union's Horizon 2020 research and innovation program
592 under grant agreement no. 642976.
593
594 **References**
595
596 Alonso-Zarza, A.M. 2003. Palaeoenvironmental significance of palustrine carbonates and calcretes in the
597 geological record. *Earth-Science Reviews*, **60**, 261–298, doi: 10.1016/S0012-8252(02)00106-X.
598 Andersen, T.B., Corfu, F., Labrousse, L. & Osmundsen, P.-T. 2012. Evidence for hyperextension along the
599 pre-Caledonian margin of Baltica. *Journal of the Geological Society*, **169**, 601–612, doi:
600 10.1144/0016-76492012-011.
601 Bach, W., Paulick, H., Garrido, C.J., Ildefonse, B., Meurer, W.P. & Humphris, S.E. 2006. Unraveling the
602 sequence of serpentinization reactions: Petrography, mineral chemistry, and petrophysics of
603 serpentinites from MAR 15°N (ODP Leg 209, Site 1274). *Geophysical Research Letters*, **33**, L13306,
604 doi: 10.1029/2006GL025681.
605 Bales, R.C. & Morgan, J.J. 1985. Dissolution kinetics of chrysotile at pH 7 to 10. *Geochimica et*
606 *Cosmochimica Acta*, **49**, 2281–2288, doi: 10.1016/0016-7037(85)90228-5.
607 Beauvais, A., Parisot, J.-C. & Savin, C. 2007. Ultramafic rock weathering and slope erosion processes in a
608 South West Pacific tropical environment. *Geomorphology*, **83**, 1–13, doi:
609 10.1016/j.geomorph.2006.06.016.
610 Beinlich, A. & Austrheim, H. 2012. In situ sequestration of atmospheric CO_2 at low temperature and surface
611 cracking of serpentinized peridotite in mine shafts. *Chemical Geology*, **332**–**333**, 32–44, doi:
612 10.1016/j.chemgeo.2012.09.015.
613 Beinlich, A., Austrheim, H., Glodny, J., Erambert, M. & Andersen, T.B. 2010. CO_2 sequestration and
614 extreme Mg depletion in serpentinized peridotite clasts from the Devonian Solund basin, SW-Norway.
615 *Geochimica et Cosmochimica Acta*, **74**, 6935–6964, doi: 10.1016/j.gca.2010.07.027.
616 Beinlich, A., Plümper, O., Hövelmann, J., Austrheim, H. & Jamtveit, B. 2012. Massive serpentinite
617 carbonation at Linnajavri, N-Norway. *Terra Nova*, **24**, 446–455, doi: 10.1111/j.1365-
618 3121.2012.01083.x.
619 Bickmore, B.R., Wheeler, J.C., Bates, B., Nagy, K.L. & Eggett, D.L. 2008. Reaction pathways for quartz
620 dissolution determined by statistical and graphical analysis of macroscopic experimental data.
621 *Geochimica et Cosmochimica Acta*, **72,** 4521–4536, doi: 10.1016/j.gca.2008.07.002.
622 Brady, P. V. & Walther, J. V. 1990. Kinetics of quartz dissolution at low temperatures. *Chemical Geology*,

82, 253–264, doi: 10.1016/0009-2541(90)90084-K.

Brehm, U., Gorbushina, A. & Mottershead, D. 2005. The role of microorganisms and biofilms in the breakdown and dissolution of quartz and glass. *Palaeogeography, Palaeoclimatology, Palaeoecology*, **219**, 117–129, doi: 10.1016/j.palaeo.2004.10.017.

Brew, D.R.M. & Glasser, F.P. 2005. Synthesis and characterisation of magnesium silicate hydrate gels. *Cement and Concrete Research*, **35**, 85–98, doi: 10.1016/j.cemconres.2004.06.022.

Cipolli, F., Gambardella, B., Marini, L., Ottonello, G. & Zuccolini, M.V. 2004. Geochemistry of high-pH waters from serpentinites of the Gruppo di Voltri (Genova, Italy) and reaction path modeling of CO_2 sequestration in serpentinite aquifers. *Applied Geochemistry*, **19**, 787–802, doi: 10.1016/j.apgeochem.2003.10.007.

Darragi, F. & Tardy, Y. 1987. Authigenic trioctahedral smectites controlling ph, alkalinity, silica and magnesium concentrations in alkaline lakes. *Chemical Geology*, **63**, 59–72, doi: 10.1016/0009-2541(87)90074-X.

Daval, D., Hellmann, R., Martinez, I., Gangloff, S. & Guyot, F. 2013. Lizardite serpentine dissolution kinetics as a function of pH and temperature, including effects of elevated pCO_2. *Chemical Geology*, **351**, 245–256, doi: 10.1016/j.chemgeo.2013.05.020.

Dewald, U. & Achternbosch, M. 2016. Why did more sustainable cements failed so far? Disruptive innovations and their barriers in a basic industry. *Environmental Innovation and Societal Transitions*, **19**, 15–30, doi: 10.1016/j.eist.2015.10.001.

Dove, P.M. & Nix, C.J. 1997. The influence of the alkaline earth cations, magnesium, calcium, and barium on the dissolution kinetics of quartz. *Geochimica et Cosmochimica Acta*, **61**, 3329–3340, doi: 10.1016/S0016-7037(97)00217-2.

Elango, L. & Kannan, R. 2007. Rock–water interaction and its control on chemical composition of groundwater. *Developments in Environmental Science*, **5**, 229–243., doi: 10.1016/S1474-8177(07)05011-5.

Frost, R.B. & Beard, J.S. 2007. On silica activity and serpentinization. *Journal of Petrology*, **48**, 1351–1368, doi: 10.1093/petrology/egm021.

Furquim, S.A.C., Graham, R.C., Barbiero, L., de Queiroz Neto, J.P. & Vallès, V. 2008. Mineralogy and genesis of smectites in an alkaline-saline environment of Pantanal wetland, Brazil. *Clays and Clay Minerals*, **56**, 579–595, doi: 10.1346/CCMN.2008.0560511.

Gac, J.Y., Droubi, A., Fritz, B. & Tardy, Y. 1977. Geochemical behaviour of silica and magnesium during the evaporation of waters in Chad. *Chemical Geology*, **19**, 215–228, doi: 10.1016/0009-2541(77)90016-X.

Genthon, P., Join, J.-L. & Jeanpert, J. 2017. Differential weathering in ultramafic rocks of New Caledonia:

The role of infiltration instability. *Journal of Hydrology*, **550**, 268–278, doi: 10.1016/j.jhydrol.2017.04.059.

Goldich, S.S. 1938. A study of rock-weathering. *The Journal of Geology*, **46**, 17–58.

Hansen, L.D., Dipple, G.M., Gordon, T.M. & Kellett, D.A. 2005. Carbonated serpentinite (listwanite) at Atlin, British Columbia: a geological analogue to carbon dioxide sequestration. *Canadian Mineralogist*, **43**, 225–239.

House, W.A. & Orr, D.R. 1992. Investigation of the pH dependence of the kinetics of quartz dissolution at 25°C. *Journal of the Chemical Society, Faraday Transactions*, **88**, 233–241.

Hänchen, M., Prigiobbe, V., Baciocchi, R. & Mazzotti, M. 2008. Precipitation in the Mg-carbonate system-effects of temperature and CO_2 pressure. *Chemical Engineering Science*, **63**, 1012–1028, doi: 10.1016/j.ces.2007.09.052.

Hövelmann, J., Austrheim, H., Beinlich, A. & Anne Munz, I. 2011. Experimental study of the carbonation of partially serpentinized and weathered peridotites. *Geochimica et Cosmochimica Acta*, **75**, 6760–6779, doi: 10.1016/j.gca.2011.08.032.

Hövelmann, J., Putnis, C.V., Ruiz-Agudo, E. & Austrheim, H. 2012. Direct nanoscale observations of CO_2 sequestration during brucite [$Mg(OH)_2$] dissolution. *Environmental Science and Technology*, **46**, 5253–5260, doi: 10.1021/es300403n.

Imbabi, M.S., Carrigan, C. & McKenna, S. 2012. Trends and developments in green cement and concrete technology. *International Journal of Sustainable Built Environment*, **1**, 194–216, doi: 10.1016/j.ijsbe.2013.05.001.

IPCC (Intergovernmental Panel on Climate Change) 2005. IPCC special report on carbon dioxide capture and storage. 1–443.

Jin, F. & Al-Tabbaa, A. 2014. Strength and hydration products of reactive MgO-silica pastes. *Cement and Concrete Composites*, **52**, 27–33, doi: 10.1016/j.cemconcomp.2014.04.003.

Kelemen, P.B. & Matter, J. 2008. In situ carbonation of peridotite for CO_2 storage. *Proceedings of the National Academy of Sciences*, **105**, 17295–17300, doi: 10.1073/pnas.0805794105.

Lasaga, A.C. 1984. Chemical kinetics of water-rock interactions. *Journal of Geophysical Research: Solid Earth*, **89**, 4009–4025, doi: 10.1029/JB089iB06p04009.

Li, Z., Zhang, T., Hu, J., Tang, Y., Niu, Y., Wei, J. & Yu, Q. 2014. Characterization of reaction products and reaction process of $MgO–SiO_2–H_2O$ system at room temperature. *Construction and Building Materials*, **61**, 252–259, doi: 10.1016/j.conbuildmat.2014.03.004.

Meunier, A. 2006. Why are clay minerals small? *Clay Minerals*, **41**, 551–566, doi: https://doi.org/10.1180/0009855064120205.

691 Moore, A.C. & Hultin, I. 1980. Petrology, mineralogy, and origin of the Feragen ultramafic body, Sor-
692 Trondelag, Norway. *Norsk Geologisk Tidsskrift*, **60**, 235–254.
693 Mumpton, F.A. & Thompson, C.S. 1966. The stability of brucite in the weathering zone of the New Idria
694 serpentinite. *Clays and Clay Minerals*, **14**, 249–257, doi: 10.1346/CCMN.1966.0140122.
695 Oskierski, H.C., Dlugogorski, B.Z. & Jacobsen, G. 2013. Sequestration of atmospheric CO_2 in a
696 weathering-derived, serpentinite-hosted magnesite deposit: 14C tracing of carbon sources and age
697 constraints for a refined genetic model. *Geochimica et Cosmochimica Acta*, **122**, 226–246, doi:
698 10.1016/j.gca.2013.08.029.
699 Plümper, O., Beinlich, A., Bach, W., Janots, E. & Austrheim, H. 2014. Garnets within geode-like
700 serpentinite veins: Implications for element transport, hydrogen production and life-supporting
701 environment formation. *Geochimica et Cosmochimica Acta*, **141**, 454–471, doi:
702 10.1016/j.gca.2014.07.002.
703 Pokrovsky, O.S. & Schott, J. 2004. Experimental study of brucite dissolution and precipitation in aqueous
704 solutions: Surface speciation and chemical affinity control. *Geochimica et Cosmochimica Acta*, **68**,
705 31–45, doi: 10.1016/S0016-7037(03)00238-2.
706 Putnis, A. 2002. Mineral replacement reactions: from macroscopic observations to microscopic
707 mechanisms. *Mineralogical Magazine*, **66**, 689–708, doi: 10.1180/0026461026650056.
708 Ratié, G., Jouvin, D., et al. 2015. Nickel isotope fractionation during tropical weathering of ultramafic rocks.
709 *Chemical Geology*, **402**, 68–76, doi: 10.1016/j.chemgeo.2015.02.039.
710 Rimstidt, J.D. 2015. Rate equations for sodium catalyzed quartz dissolution. *Geochimica et Cosmochimica*
711 *Acta*, **167**, 195–204, doi: 10.1016/j.gca.2015.07.030.
712 Roosz, C., Grangeon, S., et al. 2015. Crystal structure of magnesium silicate hydrates (M-S-H): The relation
713 with 2:1 Mg-Si phyllosilicates. *Cement and Concrete Research*, **73**, 228–237, doi:
714 10.1016/j.cemconres.2015.03.014.
715 Sauer, D., Stein, C., Glatzel, S., Kühn, J., Zarei, M. & Stahr, K. 2015. Duricrusts in soils of the Alentejo
716 (southern Portugal)-types, distribution, genesis and time of their formation. *Journal of Soils and*
717 *Sediments*, **15**, 1437–1453, doi: 10.1007/s11368-015-1066-x.
718 Schneider, M., Romer, M., Tschudin, M. & Bolio, H. 2011. Sustainable cement production-present and
719 future. *Cement and Concrete Research*, **41**, 642–650, doi: 10.1016/j.cemconres.2011.03.019.
720 Schopka, H.H., Derry, L.A. & Arcilla, C.A. 2011. Chemical weathering, river geochemistry and
721 atmospheric carbon fluxes from volcanic and ultramafic regions on Luzon Island, the Philippines.
722 *Geochimica et Cosmochimica Acta*, **75**, 978–1002, doi: 10.1016/j.gca.2010.11.014.
723 Schott, J., Brantley, S., Crerar, D., Guy, C., Borcsik, M. & Willaime, C. 1989. Dissolution kinetics of
724 strained calcite. *Geochimica et Cosmochimica Acta*, **53**, 373–382, doi: 10.1016/0016-7037(89)90389-

X.

Temuujin, J., Okada, K. & MacKenzie, K.J.D. 1998. Formation of layered magnesium silicate during the aging of magnesium hydroxide–silica mixtures. *Journal of the American Ceramic Society*, **81**, 754–756, doi: 10.1111/j.1151-2916.1998.tb02405.x.

Tosca, N. 2015. Geochemical pathways to Mg-silicate formation. *Magnesian Clays: Characterization, Origin and Applications*, **2**, 283–330.

Tosca, N.J. & Masterson, A.L. 2014. Chemical controls on incipient Mg-silicate crystallization at 25°C: Implications for early and late diagenesis. *Clay Minerals*, **49**, 165–194, doi: 10.1180/claymin.2014.049.2.03.

Tromans, D. & Meech, J.A. 2001. Enhanced dissolution of minerals: Stored energy, amorphism and mechanical activation. *Minerals Engineering*, **14**, 1359–1377, doi: 10.1016/S0892-6875(01)00151-0.

Ulven, O.I., Beinlich, A., Hövelmann, J., Austrheim, H. & Jamtveit, B. 2017. Subarctic physicochemical weathering of serpentinized peridotite. *Earth and Planetary Science Letters*, **468**, 11–26, doi: 10.1016/j.epsl.2017.03.030.

Walling, S.A. & Provis, J.L. 2016. Magnesia-based cements: A journey of 150 years, and cements for the future? *Chemical Reviews*, **116**, 4170–4204, doi: 10.1021/acs.chemrev.5b00463.

Wei, J., Yu, Q., et al. 2011. Reaction products of MgO and microsilica cementitious materials at different temperatures. *Journal of Wuhan University of Technology – Materials Science Edition*, **26**, 745–748, doi: 10.1007/s11595-011-0304-3.

Wilson, S.A., Dipple, G.M., Power, I.M., Thom, J.M., Anderson, R.G., Raudsepp, M., Gabites, J.E., Southam, G. 2009. Carbon dioxide fixation within mine wastes of ultramafic-hosted ore deposits: Examples from the Clinton Creek and Cassiar Chrysotile deposits, Canada. *Economic Geology*, **104**, 95–112, doi: 10.2113/gsecongeo.104.1.95.

Wright, V.P. & Barnett, A.J. 2015. An abiotic model for the development of textures in some South Atlantic early Cretaceous lacustrine carbonates Cretaceous. *Geological Society, London, Special Publications*, **418**, 1–11, doi: http://dx.doi.org/10.1144/SP418.3.

Zhang, T., Vandeperre, L.J. & Cheeseman, C.R. 2012. Magnesium-silicate-hydrate cements for encapsulating problematic aluminium containing wastes. *Journal of Sustainable Cement-Based Materials*, **1**, 34–45, doi: 10.1080/21650373.2012.727322.

Zhang, T., Vandeperre, L.J. & Cheeseman, C.R. 2014. Formation of magnesium silicate hydrate (M-S-H) cement pastes using sodium hexametaphosphate. *Cement and Concrete Research*, **65**, 8–14, doi: 10.1016/j.cemconres.2014.07.001.